ACS POLYMERS Au
AN OPEN ACCESS JOURNAL OF THE AMERICAN CHEMICAL SOCIETY

pubs.acs.org/polymerau

Article

Structure–Transport Properties Governing the Interplay in Humidity-Dependent Mixed Ionic and Electronic Conduction of Conjugated Polyelectrolytes

Garrett L. Grocke, Ban Xuan Dong, Aaron D. Taggart, Alex B. F. Martinson, Jens Niklas, Oleg G. Poluektov, Joseph W. Strzalka, and Shrayesh N. Patel*

Cite This: *ACS Polym. Au* 2022, 2, 275–286

Read Online

ACCESS | Metrics & More | Article Recommendations | Supporting Information

ABSTRACT: Polymeric mixed ionic-electronic conductors (MIECs) are of broad interest in the field of energy storage and conversion, optoelectronics, and bioelectronics. A class of polymeric MIECs are conjugated polyelectrolytes (CPEs), which possess a π-conjugated backbone imparting electronic transport characteristics along with side chains composed of a pendant ionic group to allow for ionic transport. Here, our study focuses on the humidity-dependent structure–transport properties of poly[3-(potassium-*n*-alkanoate) thiophene-2,5-diyl] (P3K*n*T) CPEs with varied side-chain lengths of n = 4–7. UV–vis spectroscopy along with electronic paramagnetic resonance (EPR) spectroscopy reveals that the infiltration of water leads to a hydrated, self-doped state that allows for electronic transport. The resulting humidity-dependent ionic conductivity (σ_i) of the thin films shows a monotonic increase with relative humidity (RH) while electronic conductivity (σ_e) follows a non-monotonic profile. The values of σ_e continue to rise with increasing RH reaching a local maximum after which σ_e begins to decrease. P3K*n*Ts with higher n values demonstrate greater resiliency to increasing RH before suffering a decrease in σ_e. This drop in σ_e is attributed to two factors. First, disruption of the locally ordered π-stacked domains observed through in situ humidity-dependent grazing incidence wide-angle X-ray scattering (GIWAXS) experiments can account for some of the decrease in σ_e. A second and more dominant factor is attributed to the swelling of the amorphous domains where electronic transport pathways connecting ordered domains are impeded. P3K7T is most resilient to swelling (based on ellipsometry and water uptake measurements) where sufficient hydration allows for high σ_i (1.0×10^{-1} S/cm at 95% RH) while not substantially disrupting σ_e (1.7×10^{-2} S/cm at 85% RH and 8.0×10^{-3} S/cm at 95% RH). Overall, our study highlights the complexity of balancing electronic and ionic transport in hydrated CPEs.

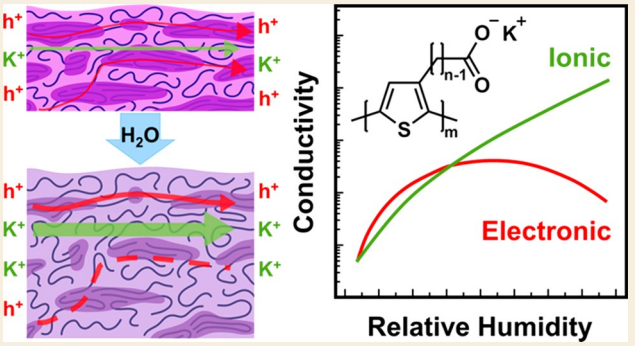

KEYWORDS: *Conjugated polyelectrolyte, mixed conduction, humidity, electronic conduction, ionic conduction, X-ray scattering*

INTRODUCTION

Materials capable of conducting both electronic and ionic charge carriers are referred to as mixed ionic-electronic conductors (MIECs) or, more simply, mixed conductors. These materials show great promise in a variety of applications, including batteries and supercapacitors, optoelectronics, bioelectronics, and electrochromic devices.[1−4] MIECs come in many forms, in both homogeneous and heterogeneous materials, which include metals, covalent inorganics such as oxides, perovskites, and ceramics, composites, and organic small molecules and polymers. Polymeric MIECs garner particular interest owed to their physical properties and synthetic tunability, enabling use in lighter, more conformable electronics. For example, the ability to transport electronic and ionic charge carriers makes polymeric MIECs valuable multifunctional binder materials in battery electrodes.[5] Polymeric materials have an inherently low thermal conductivity, making polymeric MIECs attractive candidates for electrochemical thermoelectric devices.[6,7] Additionally, their soft, flexible morphology imparts heightened biocompatibility, making them uniquely ideal for bioelectronics, such as organic electrochemical transistors (OECTs) for biosensors and neural interfaces.[8,9]

A subset of polymeric MIECs are conjugated polyelectrolytes (CPEs), polymers containing both ionically charged

Received: January 24, 2022
Revised: March 23, 2022
Accepted: March 24, 2022
Published: April 11, 2022

functional side chains, capable of associating with free ions of opposing charge, as well as a conjugated backbone capable of conducting electronic charge carriers (electrons or holes).[10−12] Wudl and co-workers synthesized and characterized polythiophenes with anionic (e.g., sulfonate) terminated side chains, now recognized as the first CPEs.[13] Overall, the library of CPEs is diverse, consisting of both *n*- and *p*-type conjugated backbones as well as cationic, anionic, and zwitterionic functional groups.[10,12,14] More advanced CPEs are a current subject of interest, with an example being "donor−acceptor" polymers, in which electron-donating and accepting moieties alternate along the backbone, which provides better control of the electronic and optical band gap and increased electronic conductivity.[15] These CPEs have been designed for interfacial layer materials in optoelectronic devices such as organic light-emitting diodes (OLEDs) and organic photovoltaics (OPV) cells. Additionally, the polar ionic character of CPEs makes them soluble in water and other polar solvents, allowing for increased processing capabilities in environmentally friendly solvents.[13]

CPEs and conjugated polymers in general are formally semiconductors and thus are electronic insulators in their pristine form. Doping either chemically or electrochemically is the common route of enabling electronic conduction. In the case of chemical *p*-doping, a small molecule dopant anion balances the hole charge carrier (polaron) on the polymer backbone. Foundational work by Wudl and co-workers on CPEs introduced the concept of so-called "self-doping."[16] In this scenario, self-doping is derived from the fact that the anionic side chains fixed along the backbone serve to balance the hole charge carriers. However, it is important to clarify that self-doping does not necessarily mean CPEs are intrinsically conductive simply from the presence of ionized side chains. An external driving force is still needed to generate electronic carriers either electrochemically or chemically. A particularly interesting aspect of these materials, the electronic transport in CPEs can be modulated through the presence of water.[16−18] In self-doped CPEs, liberation of a free cation allows the covalently bound anion to stabilize the formation of a polaronic hole charge carrier along the polymer backbone. As the free cation's ability to dissociate from the side chain is requisite for this to occur, the presence of water or other sufficiently polar solvent is a critical component of the self-doping mechanism. This phenomenon has been observed in the earliest polythiophene-based CPEs[16] to most recently by Cao et al. in which a pendant sulfonate group was shown to stabilize polaron formation in the poly[2,6-(4,4-bis-potassium butanylsulfonate-4*H*-cyclopenta-[2,1-*b*;3,4-*b*′]-dithiophene)-*alt*-4,7-(2,1,3-benzothiadiazole)] (PCPDTBT-SO_3K) donor−acceptor polymer.[19] The presence of water was demonstrated as necessary for the self-doping process, and the material was dedoped by removing water via thermal annealing.

It is a well-accepted fact that the morphology of conjugated polymers has a large impact on their charge transfer behavior.[20,21] In general, it is believed that electronic transport is optimized in the presence of sufficient chain aggregation with π-stacking (ordered domains) and sufficient interaggregate tie-chains spanning the amorphous domain. In contrast, amorphous polymers are typically needed for favorable for ionic conduction. A random, more diffuse polymer structure allows for physical passage of ionic species more readily than dense ordered arrangements, a concept well-explored in systems such as Nafion for fuel cells[22] and poly(ethylene oxide) (PEO) for lithium ion batteries.[23]

Understanding the complex role of morphology in permitting efficient mixed ionic and electronic transport in conjugated polymers remains a challenging task.[24] Many recent efforts have investigated ion transport in conjugated polymers bearing oligo(ethylene glycol) side chains, examining the impact of specific side-chain chemistry and ion selection, with a large focus on application to OECTs.[25−29] Despite these efforts, the mechanisms by which ion conduction is mediated are still less rigorously studied than their electronic counterparts. In addition, the operation of many mixed conduction-based devices commonly occurs in an aqueous media where water and ions inevitably infiltrate and impact the device performance.[27,29−31]

Recent efforts have demonstrated the impact of hydration on mixed conducting systems via control of local humidity on thin film samples. Wang et al. compared derivatives of PEDOT with varying ionic groups under humidified conditions, revealing relative humidity (RH)-dependent mixed conductivity and thermoelectric effect.[32] Merkle et al. demonstrated the ability to selectively tune ionic conductivity (σ_i) and electronic conductivity (σ_e) of a polythiophene-based anionic sulfonate CPE by modulating electronic conduction with molecular dopants and ionic conduction by varying RH.[17] More recently, Wieland et al. further investigated this phenomenon by coupling a study of water uptake in this system to the changes in conductivity, drawing comparisons to well-characterized PEDOT:PSS-Na dual-conducting and Nafion ion-conducting systems, proposing a commonality in their morphologies, with a separation of hydrophilic and hydrophobic phases, with each conducting electronic and ionic charge carriers, respectively.[33]

While the response of mixed ionic and electronic conduction characteristics of CPEs to local environment (e.g., humidity) has been detailed in studies such as those previously discussed, a more in-depth structure−property analysis of CPEs under these conditions remains the topic of ongoing investigation. In this work we report on the impact of humidity on structure and mixed conductivity for a series of conjugated polyelectrolytes poly[3-(potassium-*n*-alkanoate) thiophene-2,5-diyl] (P3K*n*T) where n = 4−7 (Figure 1). UV−vis spectroscopy and EPR

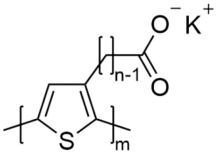

Figure 1. Chemical structure for the P3K*n*T polymer family. Polymer lot analysis can be found in the Materials and Methods section.

spectroscopy reveal that water infiltration leads to hydrated, self-doped thin films critical to enabling electronic conduction. Additionally, based on humidity-dependent ellipsometry and dynamic vapor sorption (DVS), the extent of the water uptake and swelling as a function of RH varies across the four P3K*n*T derivatives. In situ RH-dependent grazing incidence wide-angle X-ray scattering (GIWAXS) indicates that the locally ordered domains are partially disrupted from the infiltration of water. Based on electrochemical impedance spectroscopy (EIS) measurements, σ_i is found to monotonically increase with RH whereas σ_e follows a non-monotonic profile where σ_e increases until dropping at high RH. In addition to the

https://doi.org/10.1021/acspolymersau.2c00005
ACS Polym. Au 2022, 2, 275−286

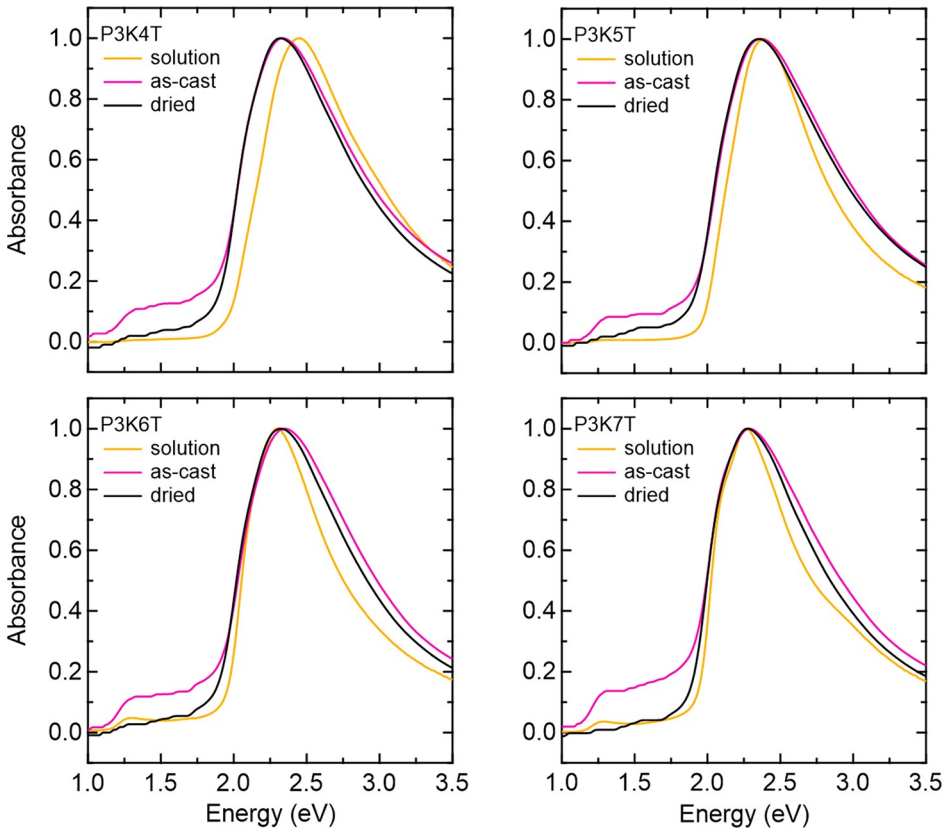

Figure 2. UV−vis of P3K*n*T solutions (4 mg/mL in DI water) as well as P3K*n*T thin films as-cast and after heating (at 60 °C for 24 h in an argon glovebox). All curves are normalized based on their peak absorbance.

disruption of locally ordered π-stacked domains, the decrease in σ_e is largely attributed to the swelling of amorphous domains where electronic transport pathways are impeded.

RESULTS AND DISCUSSION

UV−Vis Absorption Reveals π-Stacked Aggregation and Electronic Carrier Generation

UV−vis spectra of the polymer solutions and thin films reveal absorption features characteristic of both π-stacked aggregates and amorphous bands (Figure 2). Spectra do not exhibit a dramatic red shift from solution to solid state, indicating a high degree of aggregation already present in solution. A small red shift from solution to solid state is more present in shorter side-chain species, and diminishes with increasing *n*. This trend suggests that longer alkyl side chains contribute to a higher nonpolar character, resulting in a higher degree of aggregation in solution. The use of a Spano model fit identifies individual contributions of the aggregrate and amorphous regions of the polymers (Figure S1). The large absorption feature at lower energy peaking at ∼2.3 to ∼2.4 eV corresponds to the aggregates in the sample, with deconvoluted peaks associated with the 0−0, 0−1, and 0−2 vibronic transitions of π-stacked aggregates shown. The absorption feature peaking at ∼2.7−2.8 eV corresponds to disordered (amorphous) fraction of polymer chains. By visual inspection, and through deconvoluting the π-stacking peaks, we observe a low A_{0-0}/A_{0-1} ratio for all P3K*n*T species. This is indicative of the formation of H-aggregates, in which interchain $\pi-\pi$ excitonic coupling dominates. These characteristics appear to be largely preserved from solution to solid state, supporting the notion that local ordering is largely preserved as π-stacked aggregates in solution coalesce to form a solid film. Extracted values from the Spano fit for thin film samples can be found in Table S1. The polymer aggregate fraction is roughly 9% less in as-cast films compared to sufficiently dried samples, suggesting the presence of water plays a role in disrupting the ordered domains of the polymer thin film.

In the lower energy (1−2 eV) regime, absorption features indicate a sub-band gap transition characteristic of the formation of polarons (hole charge carriers). This feature is most present in the as-cast condition where more residual water remains. After the thin films are heated at 60 °C overnight in argon to remove water, the intensity of the polaronic absorption feature decreases. This feature is also visible in the solution state, being more apparent in species with a longer side chain of greater *n*. The formation of the polaronic hole charge in hydrated thin films arises from the self-doping process of conjugated polyelectrolytes described in the introduction. Here, the self-doping process arises from water molecules dissociating and solvating K^+ ions from the alkanoate side chains, and in turn allowing the negatively charged side chain to stabilize hole charge formation on the backbone brought about by protonation from the water.[19]

EPR Spectroscopy Reveals Spin Concentration Increases with Humidity

Electron paramagnetic resonance (EPR) spectroscopy experiments were performed to further verify the formation of polaronic charge carriers (unpaired spins) from the presence of water in the thin films. Experiments were performed on thin films (ca. 20 nm) cast on quartz substrates. These thins films were equilibrated under three different conditions: as-cast,

https://doi.org/10.1021/acspolymersau.2c00005
ACS Polym. Au 2022, 2, 275−286

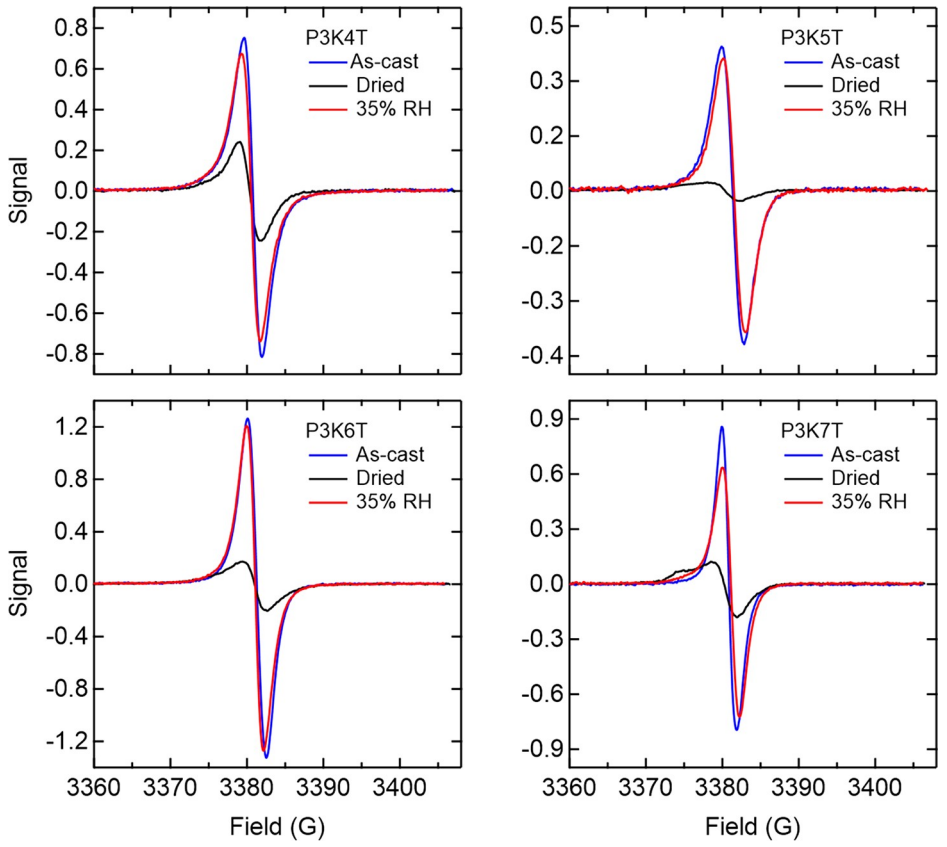

Figure 3. Continuous wave (CW) X-band EPR spectra for as-cast, dried, and rehumidified P3K*n*T films cast on quartz substrates.

dried via heating as defined previously, as well as rehydrated to 35% RH to best simulate approximate ambient conditions resulting from spin-coating. Continuous wave (CW) X-band EPR spectra are shown in Figure 3. An increase in signal from the dried state to either hydrated state is observed for all four P3K*n*T derivatives. The higher intensity arises from the presence of unpaired electrons from the polaronic charge formed by the presence of water facilitating the self-doping mechanism.

To approximate the extent of self-doping as a function of RH, a more granular quantification of the spin concentration (N) was performed for two representative derivatives: P3K4T and P3K6T. Here, EPR sample tubes were coated internally with the polymer, dried under vacuum at 60 °C overnight, and then equilibrated over a range of RH from 0 to 95%. For these samples, the EPR signal increases as a function of RH (Figure S2). The value of N at each RH was calculated through double integration of the EPR spectrum, normalized by the mass of the polymer. As shown in Figure S2b, N increases monotonically from ca. 1×10^{18} spins/g at 0% RH to ca. 3×10^{19} spins/g at 95% RH for both polymers. While small variations in N are observed between P3K4T and P3K6T, they share a common trend, wherein N is within a factor of 2. As a frame of reference, common values for N are on the order of $10^{20} - 10^{21}$ spins/g for polythiophene derivatives when extrinsically doped by a strong oxidant.[34] Therefore, the doping level (or polaronic charge carrier concentration) in P3K*n*Ts is in the lower to moderate levels across the RH range.

DVS and Ellipsometry Show the Impact of Water Uptake and Swelling with Increasing Humidity

Dynamic vapor sorption (DVS) was used to measure the water uptake (WU) level in as-received P3K*n*T polymer powders at different RH levels. The WU level increases at a relatively constant rate up to RH = 75% at approximately the same rate for the four P3K*n*T derivatives (Figure 4a). At RH = 75%, the WU level is between 25 and 30 wt %. Beyond this point, the WU level increases rapidly and is more substantial for P3K4T and P3K6T compared to P3K5T and P3K7T. At 95% RH, the WU level is 80.8% for P3K4T, 50.9% for P3K5T, 84.1% for P3K6T, and 53.3% for P3K7T. This difference appears to correlate with the size of the polymer chains, where the molecular weights (M_W) of P3K4T and P3K6T are significantly smaller than those of the other two derivatives (see Materials section). The hydration level (λ) is also calculated based on the WU level for each P3K*n*T derivative as a function of RH to provide insight on the number of water molecules per monomer (Figure S3). At RH = 25%, λ is about <1 for all four P3K*n*T derivatives. At RH = 95%, λ is about 9 for P3K4T, 6 for P3K5T, 11 for P3K6T, and 7 for P3K7T.

To account for the WU on thin film thickness, humidity-dependent ellipsometry measurements were performed for each P3K*n*T derivative. The calculated change in the thin film thickness is shown in Figure 4b. Overall, the thin film thickness change follows a similar trend to the DVS measurement where a rapid rise beyond some critical point around 75% RH can be observed. In this processed thin film configuration (consistent to subsequent X-ray scattering and conductivity measurements), a new trend can be observed when comparing the different P3K*n*Ts. An increasing n value results in a smaller

https://doi.org/10.1021/acspolymersau.2c00005
ACS Polym. Au 2022, 2, 275−286

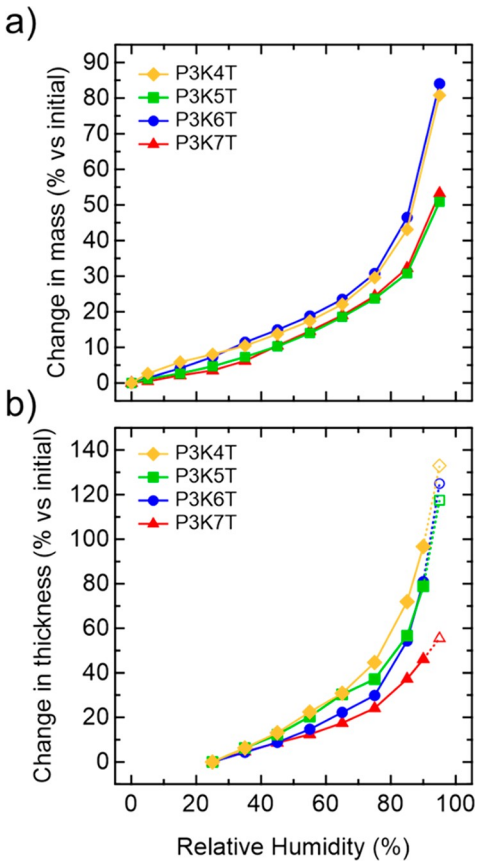

Figure 4. Responses of P3K*n*T to water sorption at increasing RH. (a) DVS curves for P3K*n*T bulk powders. (b) Change in thin film thickness as measured by ellipsometry. Values for change in thickness at 95% RH are extrapolated from best fit curves from 25% to 90% RH.

increase thin film thickness at the same RH. At RH = 90%, the change in thin film thickness is 96.7% for P3K4T, 78.9% for P3K5T, 80.9% for P3K6T, and 46.1% for P3K7T. Overall, the P3K7T thin film swells substantially less with water compared to the other P3K*n*T derivatives. Processing the polymers into thin films appears to ablate the impact of polymer M_W on uptake, and enhance the role of polymer microstructure, specifically the impact of polymer side-chain length.

Underlying Local Ordering of Dry and Humidified P3K*n*T Thin Films

It is well understood that the underlying semicrystalline microstructure comprising of nanoscale crystalline domains interconnected through the amorphous regions controls the extent of electronic charge mobility and conductivity. Here, grazing incidence wide-angle X-ray scattering (GIWAXS) was specifically used to characterize the molecular order and packing of the crystalline domains for the thin films under dry and humidified conditions. Representative 2D scattering images of dry thin films are shown in Figure 5a. Overall, all the P3K*n*T thin films exhibit similar scattering patterns that are indicative of a packing arrangement comprising π-stacked polymer backbones and interpolymer spacing along the side-chain direction. Such a molecular packing arrangement has been seen in CPEs based on donor/acceptor backbone chemistries.[7] The dehydrated 1D scattering profiles from radial integration of the 2D images are shown in Figure 5b. The most intense peak at lower q (e.g., 8.54 nm^{-1} for P3K4T) is attributed to interpolymer side-chain spacing whereas the peak at higher q (e.g., 17.78 nm^{-1} for P34KT) corresponds to π-stacking. The lower q feature shows similarities in shape and position to other CPEs bearing side chains with covalently bound anionic groups.[7] Additionally, the spacing attributed to this side-chain feature (d_{sc}) monotonically increases with side-chain aliphatic carbon number in a linear relation, with d_{sc} increasing from 0.745 nm for n = 4 to 1.15 nm for n = 7 (Figure 5c). In comparison, the π-stacking distance ($d_{\pi-\pi}$) monotonically increases similarly to d_{sc}, but to a much lower degree, with $d_{\pi-\pi}$ increasing from 0.353 for n = 4 to 0.370 nm for n = 7. These values are on the same order as other polythiophenes, including P3HT.

Humidity-Dependent GIWAXS

To study the influence of water on the molecular ordering and packing of P3K*n*Ts, RH-dependent GIWAXS experiments were performed using a custom-built RH GIWAXS chamber as shown on Figure 6a (more experimental details can be found in the Materials and Methods section, and a complete schematic can be found in Figure S4). The constraints of the experimental setup limited the RH range from 20% to 75%. Representative GIWAXS detector images of P3K*n*T films at different RH levels can be found in Figure S5a and the corresponding radial linecuts in Figure S5b. For all P3K*n*T thin films, d_{sc} increases with increasing RH (Figure 6b), with a calculated change in d_{sc} between 15 and 25% at high RH (Figure S5c). This expansion in d_{sc} indicates the ionic end groups of the side chains form hydrophilic regions within the ordered domain that preferentially absorbs water. Additionally, $d_{\pi-\pi}$ spacing is observed to increase 3.5−5% at high RH, although the change is relatively smaller compared to that of the side-chain feature expansion (Figure 6c). We posit the increase in $d_{\pi-\pi}$ arises from distortion of the conjugated backbone driven by the infiltration of the water in the side-chain domains. This distortion effect increasing $d_{\pi-\pi}$ outweighs any contraction in $d_{\pi-\pi}$ that should arise from the formation of polaronic charge along the conjugated backbone.[35] Lastly, a relative degree of crystallization (rDoC) calculation was performed on the side-chain feature of the 2D GIWAXS images (Figure S6) as a function of RH to approximate the impact of water infiltration on crystallinity. Though overall intensity and fluctuations vary from sample to sample, a common trend is observed where a linear decrease in overall rDoC is observed with increasing RH.

Humidity-Dependent Electronic and Ionic Conductivities

To determine the influence of water on the charge transport characteristics of P3K*n*T thin films, the frequency dependence of electrochemical impedance spectroscopy (EIS) is leveraged to decouple σ_i and σ_e values as a function of RH (25−95%). Thin films were deposited on custom-microfabricated interdigitated electrodes (IDEs) to achieve sufficient signal-to-noise ratio across the wide-ranging impedance of the films. Note that in the dehydrated conditions inside a dry argon-filled glovebox, the P3K*n*T thin films are highly resistive (total conductivity less than 10^{-5} S/cm). Measured conductivity arises from residual water in the film facilitating electronic charge carriers, which is consistent with results of EPR measurements (Figure S7).

Representative Nyquist plots over three different RH levels of 25%, 45%, and 65% of P3K6T thin film are shown in Figure 7. The summary of all Nyquist plots can be found in Figure S8. At all RH studied, the Nyquist plots consist of two semicircles, which is a signature of mixed ion and electron conduction.[36,37]

https://doi.org/10.1021/acspolymersau.2c00005
ACS Polym. Au 2022, 2, 275−286

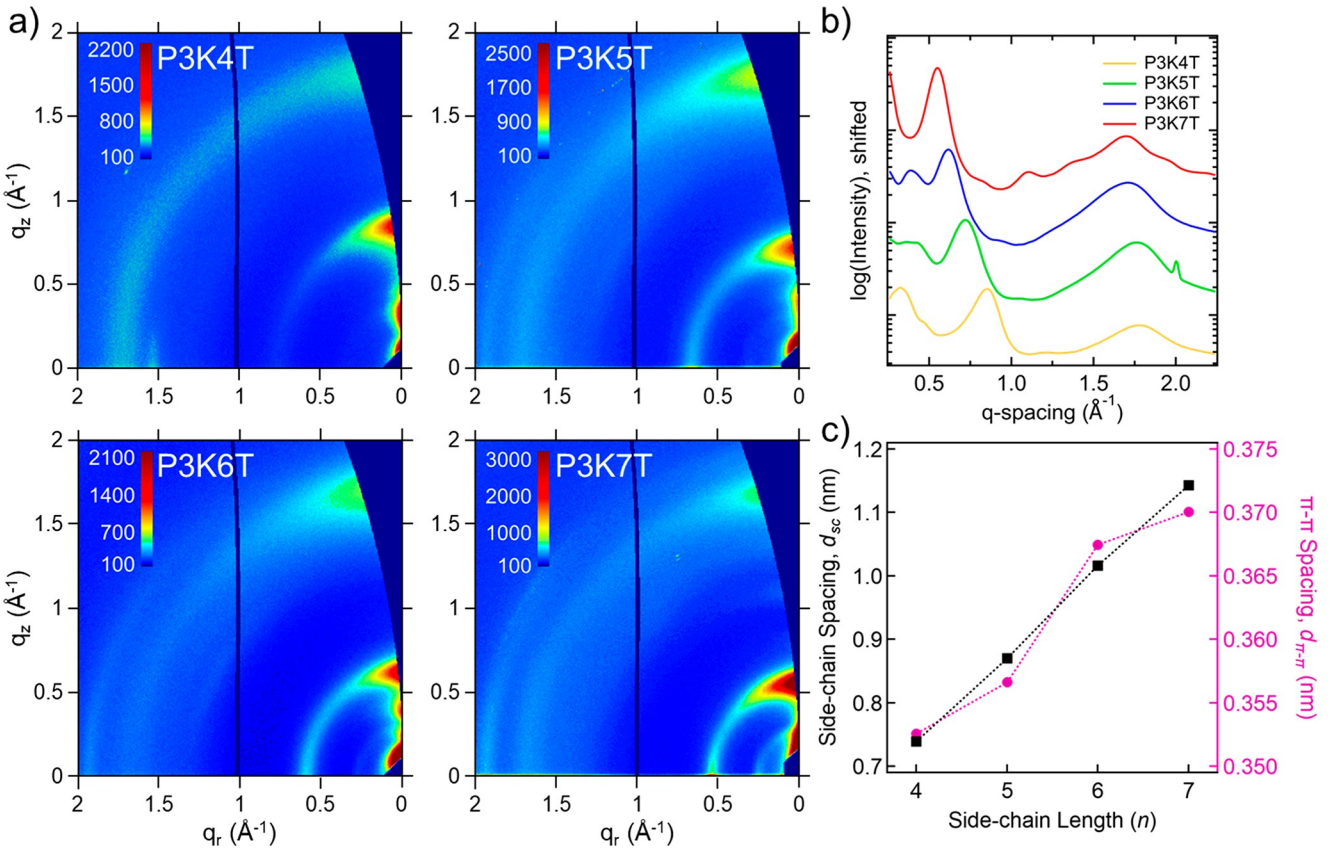

Figure 5. GIWAXS analysis of "dry" P3K*n*T thin films. (a) Example 2D images for thin films in sufficiently dehydrated condition. (b) Integrated 10° linecuts taken 80−90° from horizontal and (c) dry feature spacing peak values vs *n*.

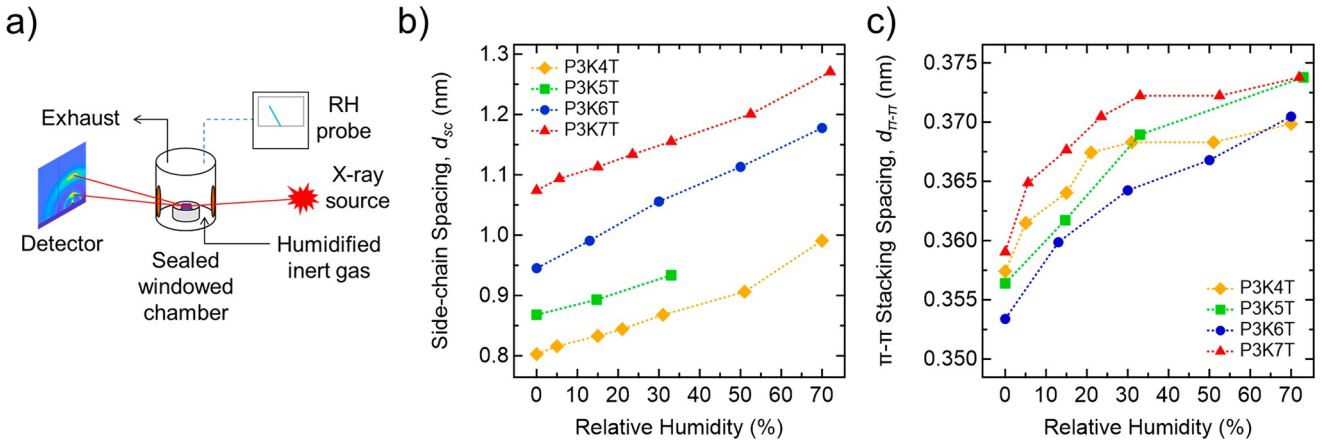

Figure 6. In situ RH-dependent GIWAXS of PKnT thin films. (a) Schematic for in situ RH-dependent GIWAXS setup. (b) Spacing for the polymer side-chain GIWAXS feature vs RH and (c) spacing for the π-stacking GIWAXS feature vs RH.

To quantify σ_i and σ_e, EIS data were fit to a simplified equivalent circuit describing parallel, simultaneous conduction of electronic and ionic charge carriers in the presence of ion-blocking electrodes, as seen in the inset of Figure 7a.[38] The radius of the first semicircle on the left reflects the combined contribution of ionic resistance (R_i) and electronic resistance (R_e) whereas the total radius of the two semicircles represent the electronic resistance R_e.[36] It is observed that as RH is increased, the radius of the first semicircle significantly reduces. However, the combined radius of both semicircles (the rightmost point) only reduces to a certain point with increasing RH, after which point it begins to expand. These two trends indicate that the ionic contribution to resistance in the system is decreasing continually with increasing RH, while the electronic resistance is initially decreasing, but then increasing after a certain RH.

Figure 7c shows σ_i of each P3K*n*T thin film as a function of RH where σ_i follows a monotonic increase across several orders of magnitude. For all P3K*n*T derivatives, the RH-dependent σ_i trend is qualitatively similar. Overall, P3K7T exhibits the highest σ_i across the full range of RH compared to other P3K*n*T derivatives. At the lowest RH of 25%, σ_i is 7.5 × 10^{-5}, 5.6 × 10^{-5}, 6.5 × 10^{-5}, and 1.5 × 10^{-4} S/cm for P3K4T, P3K5T, P3K6T, and P3K7T, respectively. At highest RH of

https://doi.org/10.1021/acspolymersau.2c00005
ACS Polym. Au 2022, 2, 275−286

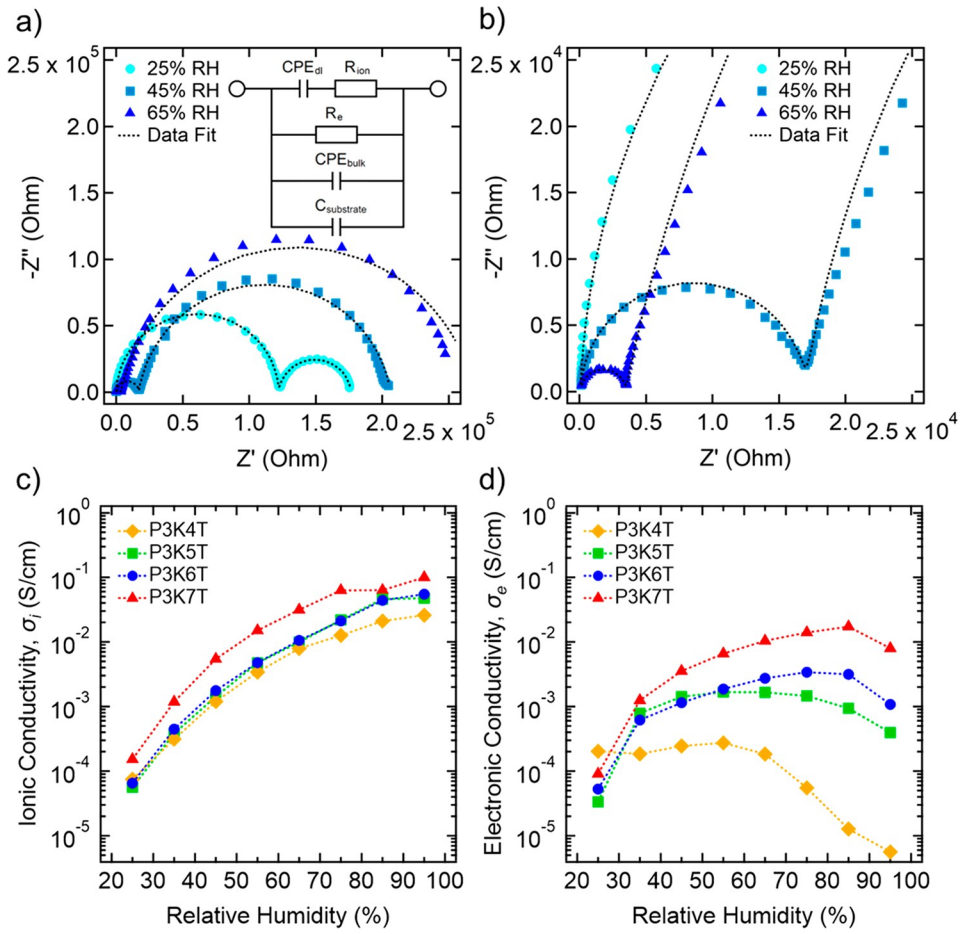

Figure 7. EIS analysis of P3K*n*T thin films on interdigitated electrodes. (a) Example Nyquist plots of P3K6T thin films on IDEs at three RH conditions with equivalent circuit used to fit EIS data and (b) expansion of the high frequency regime. (c) σ_i and (d) σ_e of P3K*n*T thin films as functions of RH.

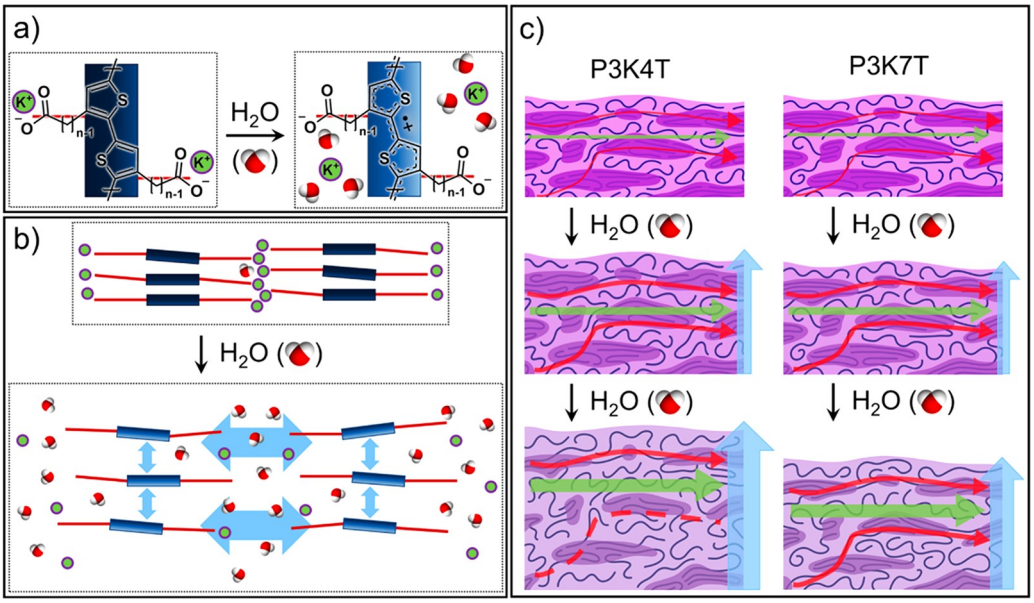

Figure 8. Schematic for influence of absorbed water on P3K*n*T thin film morphology and conductivity. (a) Water solvates potassium ions, allowing the side-chain anion to stabilize backbone hole formation. (b) Water infiltrates the ordered domains of P3K*n*T, increasing side-chain and π-stacking spacing. (c) P3K7T swells less than P3K4T at similar RH values, and increased polymer M_W allows for greater retention of interaggregate tie chains, resulting in a smaller drop in σ_e, while σ_i increases monotonically with increasing water content (red line = electronic transport pathway, green line = ionic transport pathway).

https://doi.org/10.1021/acspolymersau.2c00005
ACS Polym. Au 2022, 2, 275−286

95%, σ_i increases by nearly 4 orders of magnitude, where σ_i is 2.6×10^{-2}, 4.8×10^{-2}, 5.5×10^{-2}, and 1.0×10^{-1} S/cm for P3K4T, P3K5T, P3K6T, and P3K7T, respectively. These values σ_i are remarkably high, especially for P3K7T. For example, a benchmark material such as Nafion is reported to have a σ_i of ca. 10^{-1} S/cm at RH = 100%.[39] Other polyelectrolytes such as polystyrene sulfonic acid (PSSH) and polystyrene sodium sulfonate (PSSNa) are reported to have σ_i values ca. 1.0×10^{-3} S/cm and ca. 1.0×10^{-2} S/cm at RH = 100%, respectively.[40,41] Overall, the measured σ_i of the P3K*n*Ts are on the higher end of hydrated polyelectrolytes.

In contrast, σ_e shows a more complex behavior as a function of RH where σ_e follows a non-monotonic profile (Figure 7d). At a RH of 25%, the σ_e of all P3K*n*Ts exceeds 10^{-5} S/cm. As RH rises, σ_e increases more than an order of magnitude where σ_e is approaching and exceeding 10^{-3} S/cm for all P3K*n*Ts except for P3K4T. Notably, a decrease in σ_e is seen as RH increases and varies depending on the P3K*n*T derivative. The RH value at which σ_e begins to drop increases and the extent of the drop decreases with increasing *n* value (P3K4T to P3K7T). For P3K4T, σ_e is comparable from RH of 25% to 55% but σ_e starts to continuously drop at RH = 65% and beyond. At RH = 95%, σ_e for P3K4T has decreased by over an order of magnitude to 5.6×10^{-6} S/cm. In contrast, σ_e for P3K7T continues to increase until reaching $\sigma_e = 1.7 \times 10^{-2}$ S/cm at RH = 85%, after which σ_e decreases by a factor 2 (8×10^{-3} S/cm) at RH = 95%. Overall, as with σ_i, the values σ_e are comparatively highest for P3K7T.

Factors Influencing the Balance Between Ionic and Electronic Conduction

The results above provide insight into the structure−transport properties governing the complex interplay between ionic and electronic conduction in P3K*n*T thin films. With respect to ionic conduction, the absorbed water forms solvation shells around the potassium ion enabling dissociation from the pendant anionic side chain to generate mobile ionic carriers (Figure 8a). As the hydration level increases with RH, more cations dissociate, and the additional water forms percolating channels facilitating ionic mobility of solvated potassium ions across macroscopic length scales. Ionic conduction can occur through both the amorphous and ordered domains.[26] While the relative contribution from each domain is not known, it is reasonable to assume the amorphous domains create the easiest path for ionic conduction. Moreover, the absorbed water will plasticize the polymer to further facilitate ionic conduction. As shown with DVS and humidity-dependent thickness measurements, WU varies with P3K*n*T derivatives where the swelling is highest for P3K4T and the lowest for P3K7T. Despite their lower swelling, P3K7T exhibits the highest ionic conduction across the full RH range. We posit the longer side chain of P3K7T would exhibit faster positional dependent segmental mobility along the side chain. Here, the pendant charged moiety is farther decoupled from the rigid backbone, which allows for more efficient ion transfer.

With respect to electronic conduction, the infiltration of water controls both electronic carrier concentration (n_e) and the electronic carrier mobility (μ_e), which in total impacts the extent of σ_e as a function of RH. As noted earlier, the equilibration of thin films at different RH sets n_e through the self-doping mechanism (Figure 8a). At lower RH (<35%), the increase in charge carrier concentration outweighs any disruption in the underlying hierarchical structure that may reduce μ_e. As RH increases, the increased WU starts to disrupt the local and long-range order, which would reduce μ_e. Here, the disruption in μ_e starts to have an outsized role in controlling σ_e compared to the increase in n_e. First, based on the humidity-dependent GIWAXS results, the small expansion in $d_{\pi-\pi}$ and the reduction in crystallinity would contribute to a reduction in μ_e, and thus σ_e (Figure 8b,c). Second, as the WU level increases in the thin film, the swelling in the amorphous domain diminishes the interconnectivity of the ordered domains, interrupting electronic conduction pathways and thus reducing μ_e. This disruption of the electronic conduction pathways is the dominant factor in reducing σ_e at elevated RH. The sum of these individual factors serves to explain the non-monotonic profile of σ_e as a function of RH.

By comparing P3K4T and P3K7T, one can the see most dramatic difference in WU and thin film thickness increase on σ_e. The higher WU of P3K4T leads to substantial swelling and thus the larger separation between ordered domains (Figure 8c). Note that P3K4T has the lowest M_W and as a result would intrinsically exhibit poorer interconnectivity through interaggregate tie-chains. In total, the high level of swelling and lower M_W would have the greatest impact in impeding electronic conduction pathways for P3K4T. In contrast, P3K7T has the lowest level of swelling and thus less separation between ordered domains. Additionally, the higher M_W of P3K7T would allow for more intrinsic tie-chain interconnectivity, better preserving electronic conducting pathways across ordered and disordered (amorphous) domains.

CONCLUSIONS

In this work, factors governing the extent of simultaneous electronic and ionic conduction as a function of relative humidity on a series of P3K*n*Ts were investigated through a combination of molecular spectroscopy, water uptake analysis, X-ray scattering, and electrochemical impedance spectroscopy. UV−vis spectroscopy along with electronic paramagnetic resonance spectroscopy reveal the infiltration of water leads to hydrated, self-doped materials for all four P3K*n*Ts. This self-doping process in the presence of water is critical to generating electronic charge carriers, which increases as a function of RH. Water vapor sorption and thickness measurements via humidity-dependent ellipsometry highlight that WU level varies across the four P3K*n*Ts. P3K4T exhibited highest WU, whereas P3K7T exhibited the lowest WU throughout the full RH range. Moreover, at 90% RH, the thin film thickness (h) increased by nearly 100% for P3K4T whereas h only increased by 45% for P3K7T. To determine the effect of this WU on the local molecular order, the thin films were characterized through *in situ* humidity-dependent grazing incidence wide-angle X-ray scattering (GIWAXS). Importantly, all four P3K*n*Ts showed disruption in the local order where a monotonic expansion in the interpolymer side-chain spacing (d_{sc}) and π-stacking distance ($d_{\pi-\pi}$) were seen as a function of RH along with a decrease in crystallinity.

The resulting humidity-dependent ionic conductivity (σ_i) and electronic conductivity (σ_e) of the P3K*n*T thin films were determined through electrochemical impedance spectroscopy. σ_i shows a monotonic increase with RH. Overall, σ_i of P3K*n*Ts is quite high. At RH = 95%, P3K7T exhibited the highest σ_i of 1×10^{-1} S/cm compared to 2.6×10^{-2} S/cm for P3K4T. In contrast, the values σ_e exhibit a non-monotonic profile with RH where a drop in σ_e is seen at higher RH. For P3K4T, the $\sigma_e = 2.0 \times 10^{-4}$ S/cm at RH = 25% but drops to 5.6×10^{-6} S/cm

https://doi.org/10.1021/acspolymersau.2c00005
ACS Polym. Au 2022, 2, 275−286

at RH = 95%. On the other hand, for P3K7T, the σ_e = 9.1 × 10^{-5} S/cm at RH = 25% but continues to increase to 1.7 × 10^{-2} S/cm at RH = 85% until seeing a decrease to 8 × 10^{-3} S/cm at RH = 95%. By taking into consideration the WU and GIWAXS results, two factors are likely leading to the drop in σ_e at high RH. First, some of the decrease in σ_e as a function of RH can be attributed to the increase in $d_{\pi-\pi}$. More significantly, a second factor lies in the interruption of electronic transport pathways between ordered domains, where water absorption leads to swelling in the amorphous regions of the film and erosion of the ordered domains themselves, especially at higher RH. P3K7T is demonstrated to swell the least, allowing sufficient hydration for very high σ_i while not substantially disrupting the pathways for electronic transport across ordered and disordered (amorphous) domains. In contrast, P3K4T demonstrates the highest WU and exhibits the most substantial drop in σ_e. Overall, our study highlights inherent challenges of balancing electronic and ionic transport in hydrated CPEs. Increasing the distance between the electronically and ionically conductive regions of the CPE demonstrates a positive effect on both conduction pathways, and a higher polymer molecular weight plays a role in the retention of σ_e at RH values approaching 100%. These observations should be considered in the future synthetic design and materials processing of CPEs for applications in which absorption of water plays a critical role.

MATERIALS AND METHODS

Materials

Poly[3-(potassium-*n*-alkanoate)thiophene-2,5-diyl] polymers were purchased from Rieke Metals, with n = 4−7.[42] Polymer lot analysis was obtained from the manufacturer. P3K4T: M_W = 17−21K, RR = 89%, $Đ$ = 2.2 (M_n = 7.7−9.5k). P3K5T: M_W = 47−59K, RR = 91%, $Đ$ = 2.4 (M_n = 19.6−24.6k). P3K6T: M_W = 30−36K, RR = 88%, $Đ$ = 1.8 (M_n = 16.7−20k). P3K7T: M_W = 39−53K, RR = 93%, $Đ$ = 2.2 (M_n = 17.7−24.1k). The manufacturer claims full functionalization of alkanoate side-chain groups within analytical error. Milli-Q deionized/filtered water (18.2 MΩ·cm at 25 °C) was obtained in-house from an in-line filtration system. Anhydrous acetonitrile (>99.8%) was obtained from Sigma-Aldrich and used as received. DSC traces for dried P3K*n*T powders and TGA traces for P3K*n*T powders equilibrated at ambient conditions can be found in Figure S9. ^{1}H NMR of all species was performed at 400 MHz in a cosolvent of 2:1 D_2O and acetonitrile-d_3 (Figure S10). GPC analysis of P3K4T and P3K5T was performed in a cosolvent of 2:1 water and THF. The water contained 0.2 M $NaNO_3$ as well as phosphate buffer necessary to achieve pH = 7 (Figure S11). P3K6T and P3K7T were unable to dissolve in any available cosolvent system to a sufficient degree to obtain acceptable eluent profiles.

Solution Preparation

P3K*n*T polymers were dissolved in Milli-Q water at 60 °C for a minimum of 12 h. All solutions were prepared to a final concentration of 8 mg/mL. The solubility of different polymers varied based on polymer M_W. P3K4T and P3K6T dissolve readily, with stable solutions in concentrations exceeding 30 mg/mL. P3K5T and P3K7T, alternatively, take additional effort to dissolve, requiring prolonged heated stirring and/or cosolvents. Approximately 25% by volume acetonitrile was required to fully dissolve P3K7T. Acetonitrile was removed by heating the solution to 90 °C until the sample returned to the original mass of vial plus contents prior to acetonitrile addition.

Thin Film Casting

P3K*n*T thin films were produced via spin coating. For thin film UV−vis measurements, 0.5 mm thick z-cut quartz substrate was purchased from University Wafer. A silicon wafer with native oxide (0.5 mm, University Wafer) was used for GIWAXS measurements. In-house-designed interdigitated electrodes (IDEs) consisting of a gold electrode patterned on a passivated silicon wafer were used for EIS measurements. The IDE pattern consisted of 160 electrode "teeth" with a length of 1 mm and 8 μm spacing between each tooth. IDEs were fabricated following methodology reported by Sharon et al.[43] All substrates were cleaned using a 3-step sonication procedure, starting with acetone, followed by isopropanol, and finally Milli-Q water, for 10−15 min each. Prior to spin coating, clean substrates were exposed to air plasma under partial vacuum for 10 min in order to increase surface hydroxylation and improve wettability. A two-step spin-coating procedure was used, with a first step of 1000 rpm for 30 s followed by 3000 rpm for 60 s. Samples were dried on a heating block in an argon glovebox at 60 °C overnight to sufficiently dehydrate films. The surface topographies of the thin film samples cast on Si wafers were characterized by using a Cypher ES atomic force microscope (Asylum Research Oxford) with a FS-1500AuD cantilever at room temperature in tapping mode. Images were analyzed using the Gwyddion software package (Figure S12).

UV−Vis Spectroscopy

UV−vis measurements were performed using Shimadzu UV-3600 Plus UV−vis-NIR Dual Beam and Agilent Cary 5000 UV−vis-NIR spectrophotometers for thin film and solution measurements, respectively. Measurements were taken from a wavelength range of 250−3300 nm. Dry inert gas was flowed over the surface of dehydrated thin film samples during UV−vis measurements in order to minimize the absorption of moisture during the scan. Quartz cells of 0.1 mm short path length (Starna) were used to measure solution samples.

In Situ Humidity-Thickness Measurements

Ellipsometry was performed using a J. A. Wollam α-SE ellipsometer with a wavelength range of 380−900 nm at an angle of 70°. Samples were placed under a J. A. Woollam 500 μL liquid cell with a Viton O-ring to create a seal. The inlet and outlet ports were connected to a Linkam RH95 humidity controller, with the humidity detector downstream of the cell. A Cauchy model was fit using the CompleteEase ellipsometry software package by fitting for the thickness and parametrized optical constants that yield a minimum mean squared error (MSE). Due to the polymer's absorption around 550 nm, a multiwavelength fitting range from 650 to 900 nm was used for the transparent region. Humidity was stepped from 25% to 90% RH. Spectra were continuously collected at each humidity step until the thickness changes became minimal (typically 5−10 min). Once a steady state was reached, the final spectrum was used to calculate the thickness of the film.

Electron Paramagnetic Resonance (EPR) Spectroscopy

EPR measurements were performed at the Advanced EPR Facility at Argonne National Laboratory. CW X-band (9−10 GHz) EPR experiments were carried out with a Bruker ELEXSYS II E500 EPR spectrometer (Bruker Biospin, Rheinstetten, Germany), equipped with a TE_{102} rectangular EPR resonator (Bruker ER 4102ST). Note that the CW EPR technique uses field modulation with lock-in detection which leads to first derivative-type spectra. Measurements were performed at room temperature (T = 295 K). Data processing was done using Xepr software (Bruker BioSpin, Rheinstetten). For "as-cast/dry/35%RH" measurements, samples cast onto quartz substrates of approximately 2 mm × 15 mm were placed in quartz EPR tubes. For increasing RH samples (Figure S2), solutions were deposited in the bottom of EPR tubes and dried at 60 °C under vacuum and then equilibrated in an RH chamber before sealing. Spin quantification of a single crystal of $CuSO_4·H_2O$ with a known spin concentration was used as a reference sample. Spin quantifications were done by comparing double integrals of the experimental and reference EPR. Spin concentration was calculated based on the dry mass of the polymer deposited in the EPR tube.

https://doi.org/10.1021/acspolymersau.2c00005
ACS Polym. Au 2022, 2, 275−286

Dynamic Vapor Sorption (DVS)

DVS measurements were performed using a Surface Measurement Systems DVS Intrinsic Plus system. Approximately 20 mg samples of P3K*n*T powders were used as-received. All experiments were performed at a fixed temperature of 25 °C.

Conductivity Measurements

Electrochemical impedance spectroscopy was performed using a Gamry Reference 600 potentiostat with a frequency sweep from 1 MHz to 0.1 Hz at 100 mV vs OCP. RH was controlled using an Espec temperature and humidity chamber. Spin-coated IDEs were placed inside the chamber and connected to the potentiostat via isolated alligator clips. Samples were equilibrated with respect to absorbed moisture for extended times (greater than 1 h) prior to measurements. All samples for this work were measured at a constant temperature of 25 °C. Nyquist plots were fit to a model represented by the diagram in Figure 7a. A detailed description of IDE geometry and Nyquist plot interpretation can be found accompanying Figure S8. DC conductivity measurements of dried samples were performed in an argon glovebox on a temperature-controlled stage using a Gamry Reference 600 potentiostat to perform an $I-V$ sweep followed by linear regression of the profile to determine R_e (Figure S7).

Dry Grazing Incidence Wide-Angle X-ray Scattering (GIWAXS)

GIWAXS was used to characterize the morphology of P3K*n*T thin films. Films were spin-coated onto native oxide silicon using the previously described method. GIWAXS experiments were performed at sector 8-ID-E of the Advanced Photon Source at Argonne National Laboratory.[44] Samples were measured using an attenuated 10.92 keV beam with 10 s measurements repeated three times at different locations and then summed to improve signal-to-noise ratio. Measurements were taken at an incidence angle of 0.15°. Images were captured using a Pilatus 1MF pixel array detector (pixel size = 172 μm). Samples were measured from two different positions in order to gap-fill rows of inactive pixels between individual modules within the detector. Samples were measured over a 1-D q-range of 0–2 Å^{-1}. Dried films were measured under vacuum (10^{-3} mbar) in order to reduce air scattering and to minimize beam radiation damage. Acquired 2D intensity map images were processed using the GIXSGUI MATLAB toolbox.[45]

In Situ Humidity-Dependent GIWAXS

These experiments were performed using a custom solvent annealing chamber designed at 8-ID-E (Figure S4). Due to time constraints,% RH levels were taken at "close enough" stable values across samples (e.g., 14.7% and 15% RH). Inert gas (nitrogen or argon) was flowed into two mass flow controllers (MFC 1 and MFC 2) at empirically determined ratios, controlled via a custom software package. Gas flowed through MFC 1 then entered a sealed bubbler containing filtered deionized water before entering a mixer with gas from MFC 2. A RH probe was used to determine relative humidity of gas entering the sample chamber, and MFC ratios were adjusted manually. Pressure inside the sample chamber was approximately ambient. An aluminum frame was covered with Kapton polyimide windows to allow transmission of the X-ray beam through chamber. Substantial background scattering was present due to the relatively large volume of humidified N_2 gas in the solvent annealing chamber. A straight-line background correction was used to account for this during image analysis of humidity-dependent measurements.

Relative degree of "crystallinity" (rDoC) determination was performed using the side-chain feature with wedge cuts taken every 2° along a χ arc to account for the total sum of this feature in all orientations from fully out-of-plane (vertical) to in-plane (horizontal). A $\sin(\chi)$ correction was applied to account for the Ewald sphere intensity distortion, where χ = 0 for the out-of-plane (vertical) direction and χ = 90 for the in-plane (horizontal) direction. Each wedge cut was fit to an empirical baseline function to subtract the substantial background intensity. The background-subtracted wedge cut was then fit to a Voigt function to extract the peak position and the fwhm of the side-chain feature reflection. The resultant intensity distributions vs orientation were then integrated to get an overall intensity for the side-chain feature in each sample. The relative change in intensity was then evaluated as a function of RH for each species.

■ ASSOCIATED CONTENT

Supporting Information

The Supporting Information is available free of charge at https://pubs.acs.org/doi/10.1021/acspolymersau.2c00005.

Spano model fitting of UV–vis data, in situ EPR data, calculated hydration level data, schematic for in situ GIWAXS experiments, 2D images, linecuts, and analysis from in situ humidified GIWAXS experiments, Nyquist plots, DSC data, TGA data, DSC results, and AFM images (PDF)

■ AUTHOR INFORMATION

Corresponding Author

Shrayesh N. Patel – *Pritzker School of Molecular Engineering, University of Chicago, Illinois 60637, United States;* orcid.org/0000-0003-3657-827X; Email: shrayesh@uchicago.edu

Authors

Garrett L. Grocke – *Pritzker School of Molecular Engineering, University of Chicago, Illinois 60637, United States;* orcid.org/0000-0001-8661-5038

Ban Xuan Dong – *Pritzker School of Molecular Engineering, University of Chicago, Illinois 60637, United States;* orcid.org/0000-0002-2873-5207

Aaron D. Taggart – *Materials Science Division, Argonne National Laboratory, Lemont, Illinois 60439, United States; Advanced Materials for Energy-Water Systems Energy Frontier Research Center, Argonne National Laboratory, Lemont, Illinois 60439, United States;* orcid.org/0000-0003-4096-1351

Alex B. F. Martinson – *Materials Science Division, Argonne National Laboratory, Lemont, Illinois 60439, United States; Advanced Materials for Energy-Water Systems Energy Frontier Research Center, Argonne National Laboratory, Lemont, Illinois 60439, United States;* orcid.org/0000-0003-3916-1672

Jens Niklas – *Chemical Sciences and Engineering Division, Argonne National Laboratory, Lemont, Illinois 60439, United States;* orcid.org/0000-0002-6462-2680

Oleg G. Poluektov – *Chemical Sciences and Engineering Division, Argonne National Laboratory, Lemont, Illinois 60439, United States;* orcid.org/0000-0003-3067-9272

Joseph W. Strzalka – *X-ray Science Division, Argonne National Laboratory, Lemont, Illinois 60439, United States;* orcid.org/0000-0003-4619-8932

Complete contact information is available at: https://pubs.acs.org/10.1021/acspolymersau.2c00005

Notes

The authors declare no competing financial interest.

■ ACKNOWLEDGMENTS

This work made use of the shared facilities at the University of Chicago Materials Research Science and Engineering Center, supported by National Science Foundation under award

number DMR-2011854. Parts of this work were carried out at the Soft Matter Characterization Facility of the University of Chicago. The authors gratefully thank Dr. Xiaoying Liu for her assistance in performing DVS measurements, Dr. Zhongyang Wang for assistance in obtaining AFM images, Hongyi Zhang for guidance in NMR interpretation, and Dr. Philip Griffin for his diverse assistance throughout this study. This work made use of the Pritzker Nanofabrication Facility, which receives partial support from the SHyNE Resource, a node of the National Science Foundation's National Nanotechnology Coordinated Infrastructure (NSF ECCS-2025633). The in situ humidity-thickness measurements were supported as part of the Advanced Materials for Energy-Water Systems (AMEWS) Center, an Energy Frontier Research Center funded by the U.S. Department of Energy, Office of Science, Basic Energy Sciences. This research used resources of the Advanced Photon Source, an Office of Science User Facility operated for the U.S. Department of Energy (DOE) by Argonne National Laboratory under Contract No. DE-AC-02-06CH11357. The EPR work at Argonne National Laboratory was supported by the U.S. Department of Energy (DOE), Office of Basic Energy Sciences, Division of Chemical Sciences, Geosciences, and Biosciences, under Contract No. DE-AC-02-06CH11357.

REFERENCES

(1) Riess, I. Mixed Ionic-Electronic Conductors—Material Properties and Applications. *Solid State Ionics* **2003**, *157* (1−4), 1−17.
(2) West, A. R. Solid Electrolytes and Mixed Ionic-Electronic Conductors: An Applications Overview. *J. Mater. Chem.* **1991**, *1* (2), 157−162.
(3) Paulsen, B. D.; Tybrandt, K.; Stavrinidou, E.; Rivnay, J. Organic Mixed Ionic-Electronic Conductors. *Nat. Mater.* **2020**, *19* (1), 13−26.
(4) Rivnay, J.; Inal, S.; Collins, B. A.; Sessolo, M.; Stavrinidou, E.; Strakosas, X.; Tassone, C.; Delongchamp, D. M.; Malliaras, G. G. Structural Control of Mixed Ionic and Electronic Transport in Conducting Polymers. *Nat. Commun.* **2016**, *7* (1), 11287.
(5) Nguyen, V. A.; Kuss, C. Review—Conducting Polymer-Based Binders for Lithium-Ion Batteries and Beyond. *J. Electrochem. Soc.* **2020**, *167* (6), 065501.
(6) Russ, B.; Glaudell, A.; Urban, J. J.; Chabinyc, M. L.; Segalman, R. A. Organic Thermoelectric Materials for Energy Harvesting and Temperature Control. *Nat. Rev. Mater.* **2016**, *1* (10), 16050.
(7) Mai, C. K.; Schlitz, R. A.; Su, G. M.; Spitzer, D.; Wang, X.; Fronk, S. L.; Cahill, D. G.; Chabinyc, M. L.; Bazan, G. C. Side-Chain Effects on the Conductivity, Morphology, and Thermoelectric Properties of Self-Doped Narrow-Band-Gap Conjugated Polyelectrolytes. *J. Am. Chem. Soc.* **2014**, *136* (39), 13478−13481.
(8) Zeglio, E. Self-Doped Conjugated Polyelectrolytes for Bioelectronics Applications. Ph.D. Disseration, Linköping University, Linköping, Sweden, 2016. Linköping University Electronic Press. DOI: 10.3384/diss.diva-132731.
(9) Rivnay, J.; Inal, S.; Salleo, A.; Owens, R. M.; Berggren, M.; Malliaras, G. G. Organic Electrochemical Transistors. *Nat. Rev. Mater.* **2018**, *3* (2), 17086.
(10) Jiang, H.; Taranekar, P.; Reynolds, J. R.; Schanze, K. S. Conjugated Polyelectrolytes: Synthesis, Photophysics, and Applications. *Angew. Chemie Int. Ed.* **2009**, *48* (24), 4300−4316.
(11) Hoven, C. V.; Garcia, A.; Bazan, G. C.; Nguyen, T.-Q. Recent Applications of Conjugated Polyelectrolytes in Optoelectronic Devices. *Adv. Mater.* **2008**, *20* (20), 3793−3810.
(12) Lee, W.; Seo, J. H.; Woo, H. Y. Conjugated Polyelectrolytes: A New Class of Semiconducting Material for Organic Electronic Devices. *Polym. (United Kingdom)* **2013**, *54* (19), 5104−5121.
(13) Patil, A. O.; Ikenoue, Y.; Wudl, F.; Heeger, A. J. Water-Soluble Conducting Polymers. *J. Am. Chem. Soc.* **1987**, *109* (6), 1858−1859.
(14) Bazan, G. C.; Henson, Z. Conjugated Polyelectrolytes. In *Encyclopedia of Polymeric Nanomaterials*; Springer: Berlin, Heidelberg, 2015; pp 427−433. DOI: 10.1007/978-3-642-29648-2_4.
(15) Müllen, K.; Pisula, W. Donor-Acceptor Polymers. *J. Am. Chem. Soc.* **2015**, *137* (30), 9503−9505.
(16) Patil, A. O.; Ikenoue, Y.; Basescu, N.; Colaneri, N.; Chen, J.; Wudl, F.; Heeger, A. J. Self-Doped Conducting Polymers. *Synth. Met.* **1987**, *20* (2), 151−159.
(17) Merkle, R.; Gutbrod, P.; Reinold, P.; Katzmaier, M.; Tkachov, R.; Maier, J.; Ludwigs, S. Mixed Conductivity of Polythiophene-Based Ionic Polymers under Controlled Conditions. *Polymer (Guildf).* **2017**, *132*, 216−226.
(18) Heinze, J.; Frontana-Uribe, B. A.; Ludwigs, S. Electrochemistry of Conducting Polymers—Persistent Models and New Concepts. *Chem. Rev.* **2010**, *110* (8), 4724−4771.
(19) Cao, D. X.; Leifert, D.; Brus, V. V.; Wong, M. S.; Phan, H.; Yurash, B.; Koch, N.; Bazan, G. C.; Nguyen, T. Q. The Importance of Sulfonate to the Self-Doping Mechanism of the Water-Soluble Conjugated Polyelectrolyte PCPDTBT-SO3K. *Mater. Chem. Front.* **2020**, *4* (12), 3556−3566.
(20) Wang, H.; Xu, Y.; Yu, X.; Xing, R.; Liu, J.; Han, Y. Structure and Morphology Control in Thin Films of Conjugated Polymers for an Improved Charge Transport. *Polymers.* **2013**, *5*, 1272−1324.
(21) Noriega, R.; Rivnay, J.; Vandewal, K.; Koch, F. P. V.; Stingelin, N.; Smith, P.; Toney, M. F.; Salleo, A. A General Relationship between Disorder, Aggregation and Charge Transport in Conjugated Polymers. *Nat. Mater.* **2013**, *12* (11), 1038−1044.
(22) Ludvigsson, M.; Lindgren, J.; Tegenfeldt, J. Crystallinity in Cast Nafion. *J. Electrochem. Soc.* **2000**, *147* (4), 1303.
(23) Xue, Z.; He, D.; Xie, X. Poly(Ethylene Oxide)-Based Electrolytes for Lithium-Ion Batteries. *J. Mater. Chem. A* **2015**, *3* (38), 19218−19253.
(24) Onorato, J. W.; Luscombe, C. K. Morphological Effects on Polymeric Mixed Ionic/Electronic Conductors. *Molecular Systems Design and Engineering*. Royal Society of Chemistry April 1, 2019; pp 310−324. DOI: 10.1039/c8me00093j.
(25) Cendra, C.; Giovannitti, A.; Savva, A.; Venkatraman, V.; McCulloch, I.; Salleo, A.; Inal, S.; Rivnay, J. Role of the Anion on the Transport and Structure of Organic Mixed Conductors. *Adv. Funct. Mater.* **2019**, *29* (5), 1807034.
(26) Dong, B. X.; Nowak, C.; Onorato, J. W.; Strzalka, J.; Escobedo, F. A.; Luscombe, C. K.; Nealey, P. F.; Patel, S. N. Influence of Side-Chain Chemistry on Structure and Ionic Conduction Characteristics of Polythiophene Derivatives: A Computational and Experimental Study. *Chem. Mater.* **2019**, *31* (4), 1418−1429.
(27) Flagg, L. Q.; Bischak, C. G.; Onorato, J. W.; Rashid, R. B.; Luscombe, C. K.; Ginger, D. S. Polymer Crystallinity Controls Water Uptake in Glycol Side-Chain Polymer Organic Electrochemical Transistors. *J. Am. Chem. Soc.* **2019**, *141* (10), 4345−4354.
(28) Schmode, P.; Savva, A.; Kahl, R.; Ohayon, D.; Meichsner, F.; Dolynchuk, O.; Thurn-Albrecht, T.; Inal, S.; Thelakkat, M. The Key Role of Side Chain Linkage in Structure Formation and Mixed Conduction of Ethylene Glycol Substituted Polythiophenes. *ACS Appl. Mater. Interfaces* **2020**, *12* (11), 13029−13039.
(29) Savva, A.; Cendra, C.; Giugni, A.; Torre, B.; Surgailis, J.; Ohayon, D.; Giovannitti, A.; McCulloch, I.; Di Fabrizio, E.; Salleo, A.; et al. Influence of Water on the Performance of Organic Electrochemical Transistors. *Chem. Mater.* **2019**, *31* (3), 927−937.
(30) Zhang, S.; Kumar, P.; Nouas, A. S.; Fontaine, L.; Tang, H.; Cicoira, F. Solvent-Induced Changes in PEDOT:PSS Films for Organic Electrochemical Transistors. *APL Mater.* **2015**, *3* (1), 014911.
(31) Kim, S. M.; Kim, C. H.; Kim, Y.; Kim, N.; Lee, W. J.; Lee, E. H.; Kim, D.; Park, S.; Lee, K.; Rivnay, J.; et al. Influence of PEDOT:PSS Crystallinity and Composition on Electrochemical Transistor Performance and Long-Term Stability. *Nat. Commun. 2018 91* **2018**, *9* (1), 1−9.

(32) Wang, H.; Ail, U.; Gabrielsson, R.; Berggren, M.; Crispin, X. Ionic Seebeck Effect in Conducting Polymers. *Adv. Energy Mater.* **2015**, *5* (11), 1500044.
(33) Wieland, M.; Dingler, C.; Merkle, R.; Maier, J.; Ludwigs, S. Humidity-Controlled Water Uptake and Conductivities in Ion and Electron Mixed Conducting Polythiophene Films. *ACS Appl. Mater. Interfaces* **2020**, *12* (5), 6742−6751.
(34) Kang, K.; Schott, S.; Venkateshvaran, D.; Broch, K.; Schweicher, G.; Harkin, D.; Jellett, C.; Nielsen, C. B.; McCulloch, I.; Sirringhaus, H. Investigation of the Thermoelectric Response in Conducting Polymers Doped by Solid-State Diffusion. *Mater. Today Phys.* **2019**, *8*, 112−122.
(35) Liu, W.; Müller, L.; Ma, S.; Barlow, S.; Marder, S. R.; Kowalsky, W.; Köhn, A.; Lovrincic, R. Origin of the π-π Spacing Change upon Doping of Semiconducting Polymers. *J. Phys. Chem. C* **2018**, *122* (49), 27983−27990.
(36) Patel, S. N.; Javier, A. E.; Stone, G. M.; Mullin, S. A.; Balsara, N. P. Simultaneous Conduction of Electronic Charge and Lithium Ions in Block Copolymers. *ACS Nano* **2012**, *6* (2), 1589−1600.
(37) Dong, B. X.; Liu, Z.; Misra, M.; Strzalka, J.; Niklas, J.; Poluektov, O. G.; Escobedo, F. A.; Ober, C. K.; Nealey, P. F.; Patel, S. N. Structure Control of a π-Conjugated Oligothiophene-Based Liquid Crystal for Enhanced Mixed Ion/Electron Transport Characteristics. *ACS Nano* **2019**, *13* (7), 7665−7675.
(38) Huggins, R. A. Simple Method to Determine Electronic and Ionic Components of the Conductivity in Mixed Conductors a Review. *Ionics (Kiel).* **2002**, *8* (3−4), 300−313.
(39) Sone, Y.; et al. Proton Conductivity of Nafion 117 as Measured by a Four-Electrode AC Impedance Method. *J. Electrochem. Soc.* **1996**, *143* (4), 1254.
(40) Wee, G.; Larsson, O.; Srinivasan, M.; Berggren, M.; Crispin, X.; Mhaisalkar, S. Effect of the Ionic Conductivity on the Performance of Polyelectrolyte- Based Supercapacitors. *Adv. Funct. Mater.* **2010**, *20* (24), 4344−4350.
(41) Malti, A.; Edberg, J.; Granberg, H.; Khan, Z. U.; Andreasen, J. W.; Liu, X.; Zhao, D.; Zhang, H.; Yao, Y.; Brill, J. W.; et al. An Organic Mixed Ion-Electron Conductor for Power Electronics. *Adv. Sci.* **2016**, *3* (2), 1500305.
(42) Kim, S. H.; Kim, J. G. Preparation of Water Soluble Polythiophenes Mediated by Highly Active Zinc. *Bull. Korean Chem. Soc.* **2009**, *30* (10), 2283−2286.
(43) Sharon, D.; Bennington, P.; Liu, C.; Kambe, Y.; Dong, B. X.; Burnett, V. F.; Dolejsi, M.; Grocke, G.; Patel, S. N.; Nealey, P. F. Interrogation of Electrochemical Properties of Polymer Electrolyte Thin Films with Interdigitated Electrodes. *J. Electrochem. Soc.* **2018**, *165* (16), H1028−H1039.
(44) Jiang, Z.; Li, X.; Strzalka, J.; Sprung, M.; Sun, T.; Sandy, A. R.; Narayanan, S.; Lee, D. R.; Wang, J. The Dedicated High-Resolution Grazing-Incidence X-Ray Scattering Beamline 8-ID-E at the Advanced Photon Source. *J. Synchrotron Radiat.* **2012**, *19* (4), 627−636.
(45) Jiang, Z. GIXSGUI: A MATLAB Toolbox for Grazing-Incidence X-Ray Scattering Data Visualization and Reduction, and Indexing of Buried Three-Dimensional Periodic Nanostructured Films. *J. Appl. Crystallogr.* **2015**, *48* (3), 917−926.

https://doi.org/10.1021/acspolymersau.2c00005
ACS Polym. Au 2022, 2, 275−286